



# Stabilized microparticle aggregates of oxygen-containing nanoparticles in kerosene for enhanced droplet combustion



Philip M. Guerieri, Rohit J. Jacob, Jeffery B. DeLisio, Miles C. Rehwoldt, Michael R. Zachariah\*

University of Maryland, College Park, MD 20740, United States

## ARTICLE INFO

### Article history:

Received 1 May 2017

Revised 27 June 2017

Accepted 30 August 2017

Available online 16 October 2017

### Keywords:

Metal oxides

Nitrocellulose

Electrospray

Fuel additives

Droplet combustion

## ABSTRACT

Metallizing and gelling hydrocarbons has received attention since the 1960s, but slurry fuels utilizing micron particles suffer from long particle burning times and problematic agglomeration. This study investigates single droplet combustion of kerosene with oxygen-containing nanoparticle additives, assembled by electrospray into nitrocellulose (NC)-bound composite “mesoparticle” (MP) structures (on the order of 5  $\mu\text{m}$ ). We find significantly improved dispersion properties of these materials compared to unassembled nanoparticles. Droplet combustion is characterized with a free-falling droplet experiment utilizing high speed videography. The MP pre-assembly strategy demonstrated previously by this group to improve burning rate effects and suspension stability of nanoaluminum is extended to oxygen-containing nanoparticles of CuO, KIO<sub>4</sub>, MgO, and Al<sub>2</sub>O<sub>3</sub> added to kerosene as NC-bound MPs. Burning rate enhancements of up to 40% are seen for CuO and KIO<sub>4</sub> MPs. Direct observation of droplet combustion disruptions is used to propose active mechanisms for each additive.

© 2017 Published by Elsevier Inc. on behalf of The Combustion Institute.

## 1. Introduction

The application of various propulsion methods is limited by the operating envelope of the flight vehicle and energy source utilized [1]. Air-breathing propulsion, for instance, can deliver a higher specific impulse than rockets by utilizing atmospheric oxygen instead of an on-board oxidizer, but cannot operate outside specific flight envelopes without ample oxygen delivery to the engine [1–2]. Such technological limitations on propulsion can be mitigated by modifying the combustion properties of fuels and propellants available to vehicle engineers. Namely, increasing the volumetric energy density of liquid fuels/propellants with the addition of solid particles has received attention since proposed in 1962 [3]. However, subsequent investigations examining slurry fuels of micron-sized metal powders in combustible liquids demonstrated deleterious agglomeration effects which caused low burning rates and poor combustion efficiencies [4].

Nanoscale energetic powders are known to overcome weaknesses of their micron-scale counterparts, including reducing ignition delay and increasing reaction rates by increasing the surface-to-volume ratio of the material [5]. Nanoparticles (“NPs”) are also better suited to liquid incorporation wherein Brownian motion and

repulsive electrostatic forces can prevent gravitational settling of the additives in the fluid [3]. This has prompted increased research efforts over the last decade on NPs suspended in combustible liquids. NO<sub>x</sub>, hydrocarbon, and CO emissions can be decreased in diesel engines with NPs of Al [6–8], Al<sub>2</sub>O<sub>3</sub> [7], Fe [8], B [8], CeO<sub>2</sub> [9], Fe<sub>3</sub>O<sub>4</sub> [10], and Carbon Nanotubes (CNT) [11]. Metal oxide NPs have also been employed as oxygen carriers for direct oxidation of JP-10 in an atomized flow reactor [12]. Nanoaluminum (“nAl”) is known to reduce the ignition delay of JP-8 [13] and increase the specific impulse of JP-10 [14], and nitromethane burning rates can be increased by the addition of various nanomaterials including functionalized graphene sheets [1], silica [2,15], AlOOH [1], Al<sub>2</sub>O<sub>3</sub> [15], or nAl [2,16].

Recent studies examining single-droplet combustion and evaporation of nAl-laden fuels have identified beneficial mechanisms of these additives including radiative absorption of the particles from the flame, increased heat of combustion, and physical droplet disruptions promoting mixing and secondary atomization [17–22]. However, particle agglomeration persists as a detrimental side effect of NPs in suspension [17,20,23–26]. Long-term stability can be improved with surface modification agents; e.g. trioctylphosphine oxide (TOPO), oleic acid, or sorbitol oleate [14,5,27].

Observations show that physical droplet disruptions during evaporation or combustion upon nAl addition are common and thought to disrupt agglomerate formation and inhibit shell growth [26,27]. Miglani and Basu found that higher particle loadings

\* Corresponding author.

E-mail address: [mrz@umd.edu](mailto:mrz@umd.edu) (M.R. Zachariah).

suppressed gas ejections which were observed more frequently for low particle loadings, suggesting that a feedback loop exists between formation of agglomerate shells and resulting droplet disruptions that can dismantle them [26]. Including nitrocellulose (“NC”) as a gas-generating co-additive with nAl in kerosene has also been shown to promote droplet disruptions and increase burning rate constants of nAl-laden droplets [27].

We have previously reported that nitrocellulose can be used to assemble nanoparticles into porous agglomerate “mesoparticles” (MPs) on the order of 1–10  $\mu\text{m}$  in size which exhibit enhanced combustion compared to nAl [28]. The strategy was extended to thermite mixtures [29] demonstrating a three-fold increase in constant volume combustion pressure rise and pressurization rate for nAl/CuO MPs compared to physical mixtures. This effect was attributed to more intimate contact of the fuel and oxidizer and gas generation by NC decomposition dispersing the reactant particles thereby mitigating reactive sintering [29]. The mechanism of primary particle dispersion to mitigate sintering and promote high burning rates was supported by aerosol-based combustion observations in [30] and MPs were employed in solid rocket propellant in [31]. This MP architecture has been used to preassemble nAl for addition to kerosene, showing significantly increased suspension stability, higher maximum stable loadings, and therefore greater maximum burning rate increases versus physical mixtures of nAl and NC nanoparticles [27]. This study evaluates effects of oxygen-containing solid particles of CuO, KIO<sub>4</sub>, MgO, and Al<sub>2</sub>O<sub>3</sub> on the single-droplet combustion of kerosene in a free-droplet configuration when the same gas-generating NC co-additive and MP preassembly strategy is employed to promote droplet disruption, agglomerate break-up, and suspension stability.

## 2. Experimental

### 2.1. Nanofuel preparation

Samples tested in this study were chosen to investigate oxide compounds of various natures: CuO, a metal oxide commonly used in thermite mixtures which thermally decomposes to release oxygen; KIO<sub>4</sub>, a periodate salt more recently demonstrated as a strong oxidizer of reactive metals which also releases oxygen by thermal decomposition [32]; MgO, a metal oxide expected to be more stable than CuO but which has some possibility of oxidizing combustion species; and Al<sub>2</sub>O<sub>3</sub>, a stable metal oxide expected to be inert.

Nanopowders of CuO, MgO, and Al<sub>2</sub>O<sub>3</sub> were used as-received from Sigma-Aldrich which specified <50 nm particle sizes for all three materials (Sigma-Aldrich 544868, 549649, and 544833, respectively). SEM images shown in Fig. S1 (in Supporting information) confirm primary particle sizes on the order of 50 nm, but show secondary particle agglomerate sizes of 0.5–5  $\mu\text{m}$  for CuO and 1–10  $\mu\text{m}$  for MgO and Al<sub>2</sub>O<sub>3</sub> within tertiary fractal aggregates on the order of 50–100  $\mu\text{m}$ . KIO<sub>4</sub> nanoparticles were synthesized by spray-drying as-received KIO<sub>4</sub> (Sigma-Aldrich 210056) dissolved at 4 mg/mL in deionized water from a venturi-style collision atomizer through a silica diffusion dryer into a tube furnace at 200 °C and was collected with an in-line 400  $\mu\text{m}$  membrane filter [33]. Resulting particles are on the order of 0.1–1  $\mu\text{m}$  primary particles in agglomerates of 0.5–10  $\mu\text{m}$ . NC nanoparticles required for NC-only control samples were assembled by spray drying precursor, composed of NC collodion (Fluka Analytical 09986) diluted with acetone to approximately 25 mg/mL NC solids, into two in-line tube furnaces at 80 °C and collecting the particles in a 400  $\mu\text{m}$  membrane filter heated to 90 °C to prevent solvent condensation.

Nitrocellulose-bound mesoparticles were assembled using electro-spray particle synthesis described by Wang et al. [28] wherein precursors of solid particles suspended in NC solutions (3:1 ethanol:ether solvent) are agitated in a sonication bath for 1 h

**Table 1**

Sample mass loadings tested by mixing with 0.3 mL of kerosene including 50 mg/mL TOPO surfactant. Control samples (not shown) included neat kerosene, kerosene with TOPO surfactant, and NC nanoparticles in kerosene/TOPO at loadings of 2–10 mg/mL. Oxygen molarity defined by the oxygen content of the oxides in the final nanofuel suspensions.

		A	B	C	D
Oxygen molarity		0.44	0.89	1.33	1.78
Sample		Mass loadings (mg/mL)			
1	CuO NPs	35.4	70.8	106.1	141.5
2	KIO <sub>4</sub> NPs	25.6	51.1	76.7	102.3
3	MgO NPs	17.9	35.9	53.8	71.7
4	Al <sub>2</sub> O <sub>3</sub> NPs	15.1	30.2	45.3	60.5
5	CuO/NC MPs (6.4 wt% NC)	37.8	75.5	113.3	151.1
6	KIO <sub>4</sub> /NC MPs (6.7 wt% NC)	27.4	54.9	82.3	109.8
7	MgO/NC MPs (7.7 wt% NC)	19.4	38.8	58.2	77.6
8	Al <sub>2</sub> O <sub>3</sub> /NC MPs (8.1 wt% NC)	16.4	32.9	49.3	65.8

and magnetically stirred for 24 h before injection via syringe at 2.5 mL/h through a 0.43 mm ID stainless steel probe needle charged at 10 kV, 10 cm from and perpendicular to the probe needle, an aluminum foil collection substrate is charged to –10 kV to induce fluid breakup at the needle exit into microdroplets of precursor which dry in flight before deposition on the foil.

Nanofuel suspensions are mixed by adding NPs or MPs to 0.3 mL of kerosene (Sigma-Aldrich 329460, reagent grade) with 15 mg of trioctylphosphine oxide (TOPO) surfactant, agitating by sonication bath, and magnetically stirring for approximately 24 h immediately before combustion trials. Sonication bath times were 1 h for NP suspensions and 5 min for MP suspensions to limit possible MP damage while maximizing NP aggregate disassembly and suspension. TOPO surfactant is required to chemically stabilize particles in suspension and was proposed for this purpose by E et al. to stabilize boron in JP-10 in [14] and has successfully stabilized nAl/NC MPs [27]. To simplify comparison of nanofuel burning rates using one common control, constant TOPO concentration (50 mg/mL), nanofuel batch size (0.3 mL), and mixing/storage vial size (0.5 Dr) was maintained for all samples in this study. Each sample was removed from stirring and sonicated for 1 min prior to combustion experiment trials to ensure particle dispersion. The loadings of samples tested are shown in Table 1, which were based on equal oxygen content of the additives, constant for each loading category A–D (except for NC binder-only control samples which do not include oxides). NC binder mass throughout the study is five weight percent of the theoretical reactive mixture, i.e. 5 wt% of a stoichiometric mixture of the oxygen-containing nanoparticles and nAl fuel for direct comparison with past and planned companion studies [27].

### 2.2. Combustion characterization

Measurements of burning rate constants were taken using a apparatus described in previous studies [34,27]. Nanofuel droplets approximately 600  $\mu\text{m}$  in diameter free-fall past two methane diffusion flame igniters within a 5 × 5 × 20-in. tower filled with oxygen gas at room temperature. A magnified shadowgraph of droplets passing the igniters using an expanded HeNe laser is imaged with a high-speed camera to record initial droplet diameters ( $\pm 0.01$  mm estimated uncertainty) while a second high-speed camera captures the flame emission of the droplet over its entire burning time. By assuming full combustion of the droplets (supported by product particle capture [34,27]) such that the final diameter is taken to be zero, the burning rate constant is calculated for each droplet using Eq. (1),

$$K = \frac{1 - D_{\text{Extinction}}^2/D_0^2}{t_{\text{Extinction}}/D_0^2} \cong \frac{D_0^2}{t_{\text{Extinction}}} \quad (1)$$

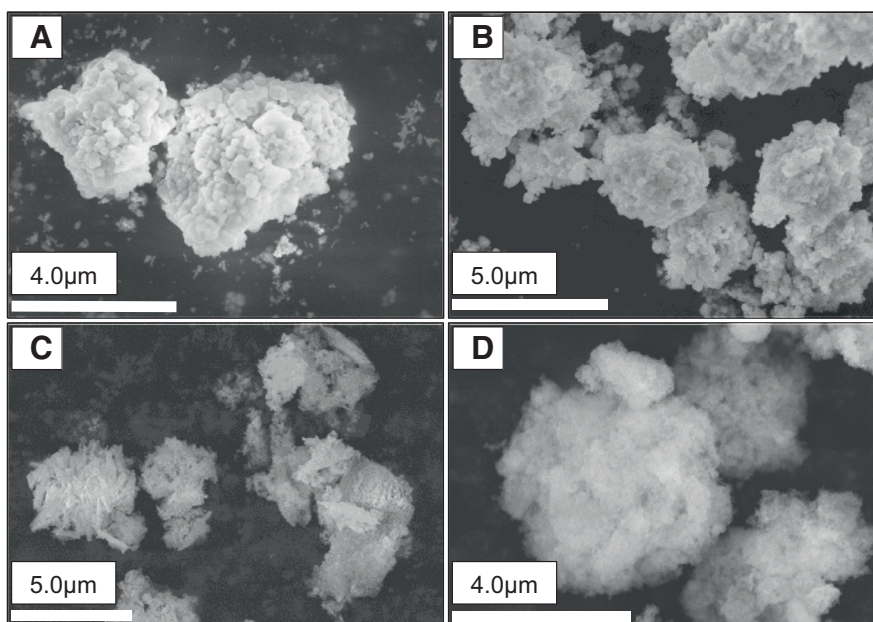


Fig. 1. SEM of electrospay assembled mesoparticles (A) CuO, (B)  $\text{KIO}_4$ , (C) MgO, and (D)  $\text{Al}_2\text{O}_3$ .

This measurement avoids distortions that solid additives cause to classical  $d^2$ -law based measurements, which rely on tracking the cross-sectional area of the droplet during combustion to assess the diameter over time, from which the burning rate constant is calculated. In such classical measurements, the volume of the droplet must be directly proportional to the mass of unreacted fuel remaining, which is generally true for a pure hydrocarbon droplet. Introducing particles however is known to induce gas generation, droplet inflations, shape distortion, and eruptions during combustion which uncouples droplet volume from unreacted mass, rendering this classical analysis inapplicable. To overcome these limitations, the burning-time based measurement used here sacrifices per-droplet precision of the classical measurement, thus requiring 8–12 droplets per trial and 2–4 repeated trials to assess  $K$  for a given sample with an estimated experimental uncertainty of  $\pm 0.1 \text{ mm}^2/\text{s}$ .

For further characterization of droplet disruptions, select samples were observed with magnified high speed video at the height of the annotation line in Fig. 3. Point spectroscopy was also taken using an Ocean Optics USB2000 + UV-VIS spectrometer with a fiber optic focused at the same height as the camera on the falling droplets. The integration time of the spectrometer was longer than the time of a droplet falling through the field of view resulting in one spectra per falling droplet. Representative spectra are shown in Figs. S6–S11.

### 3. Results and discussion

#### 3.1. Material characterization

Electrosprayed MPs are shown in SEM images in Fig. 1. MP sizes are on the order of  $5 \mu\text{m}$  and generally round which, compared to the  $\sim 1\text{--}10 \mu\text{m}$  amorphous secondary aggregates of the source oxide particles shown in Fig. S1, suggests that sonication and mixing of the electrospay precursors successfully breaks secondary soft aggregates to intimately mix NC binder with collections of primary particles  $< 5 \mu\text{m}$  in size, which reform round MPs as precursor droplets evaporate during electrospay.

Simultaneous thermogravimetric analysis and differential scanning calorimetry (TGA/DSC) was conducted to assess the thermal

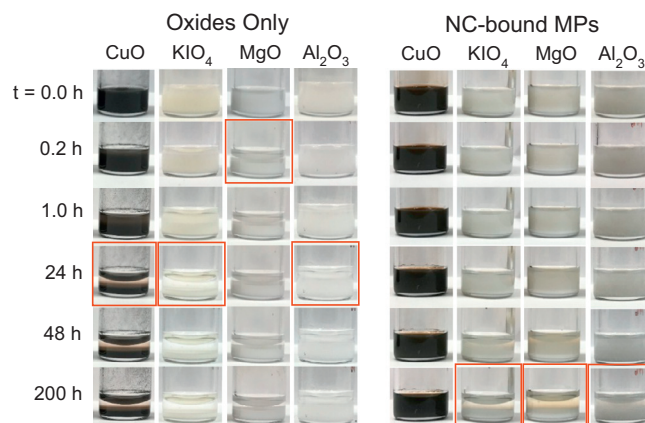
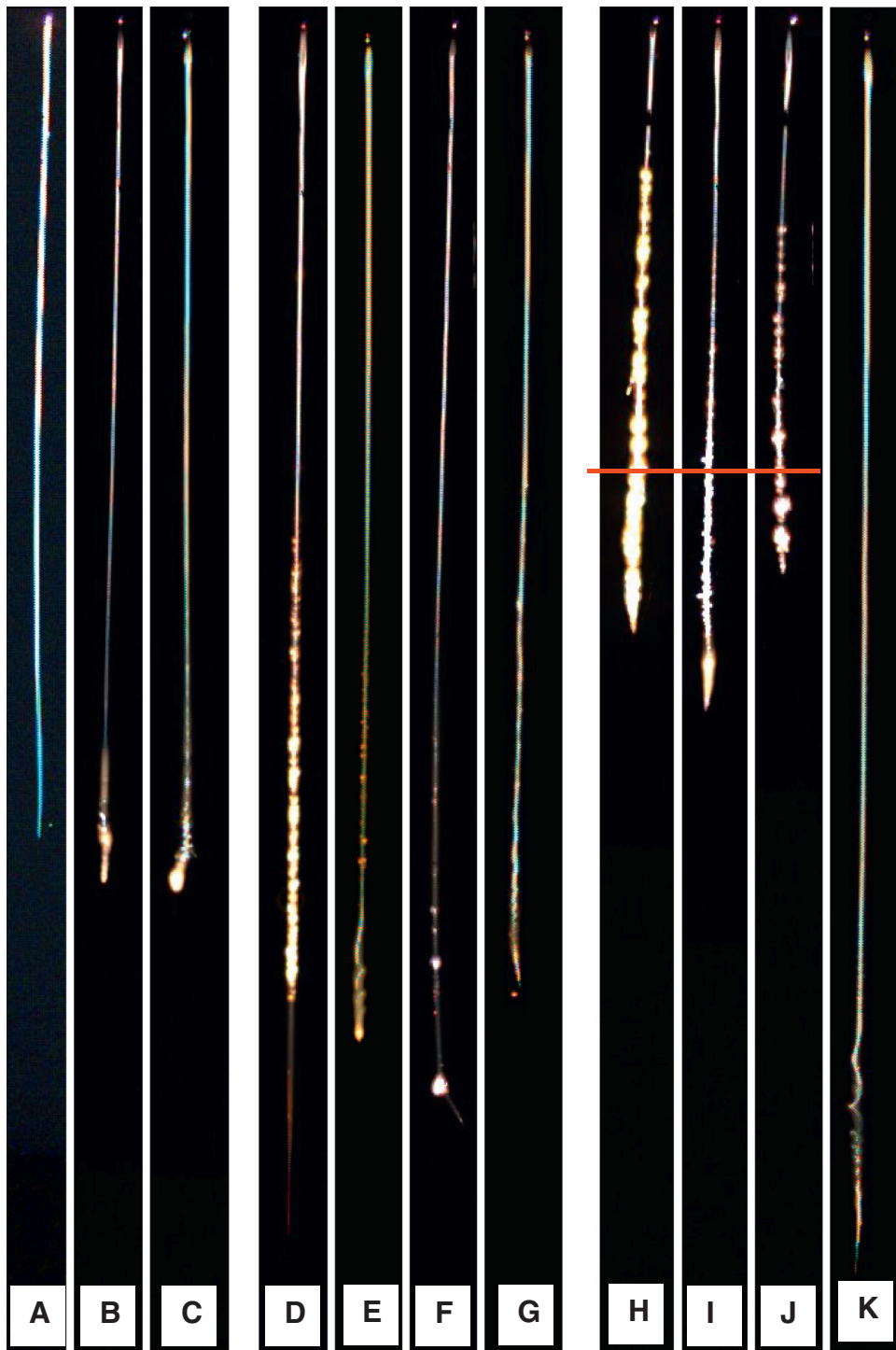


Fig. 2. Nanofuel suspension photographs at various elapsed times from dispersion by sonication. Boxed frames indicate suspensions which have visibly gravitationally settled.

behavior of the MP constituent materials, shown in Fig. S3. The NC binder decomposes exothermically at  $\sim 485 \text{ K}$ . TGA/DSC on the specific CuO nanoparticles used in this study under  $10 \text{ K min}^{-1}$  heating in argon shows onset of endothermic oxygen release at  $\sim 1100 \text{ K}$ . Jian et al. showed this CuO decomposition temperature is heating rate dependent and identified  $\text{O}_2$  release temperatures between approximately  $925 \text{ K}$  and  $1020 \text{ K}$  for heating rates of  $\sim 1.5 \times 10^5$  and  $\sim 6 \times 10^5 \text{ K s}^{-1}$ , respectively [32]. TGA/DSC of  $\text{KIO}_4$  closely matches the results of [35] with two decomposition steps at  $604 \text{ K}$  and  $830 \text{ K}$ . Conversely, TGA/DSC of MgO nanoparticles revealed only a  $\sim 2.5\%$  weight loss near  $580 \text{ K}$ , likely decomposition of impurities in as-received MgO, with no obvious thermal decomposition of the oxide below  $1200 \text{ }^\circ\text{C}$ . NC-bound MP samples show superimposed activity of both the NC binder oxide particle, exhibiting no effect of one component on the thermal behavior of the other.

The suspension stabilities are shown in Fig. 2 as a function of time after sonication. The important result here is that mesoparticles offer considerably greater colloidal stability than the corresponding unassembled materials, consistent with our observations for nAl/NC MPs in a previous study [27].



**Fig. 3.** (A) Kerosene only, (B) kerosene with TOPO surfactant (base liquid for C–H), (C) NC particles only, (D) CuO only, (E) KIO<sub>4</sub> only, (F) MgO only, (G) Al<sub>2</sub>O<sub>3</sub> only, (H) CuO/NC MPs, (I) KIO<sub>4</sub>/NC MPs, (J) MgO/NC MPs, (K) Al<sub>2</sub>O<sub>3</sub>/NC MPs. Corresponds to the height at which the magnified videos shown in Section 3.4 (and flame emission spectra shown in Fig. S6) were taken: 4.5 in. below the ignition point. (For interpretation of the references to color in this figure legend, the reader is referred to the web version of this article.)

### 3.2. Nanofuel falling droplet combustion

Figure 3 depicts representative time-lapse images of a single combustive droplet for the highest loading class of each sample (including neat kerosene without surfactant which was artificially brightened for visibility). The droplet position is not linearly related to its burning time and the initial droplet diameters can vary  $\pm 0.1$  mm, therefore the length of the traces only loosely il-

lustrates the burning rate of each sample (more accurately quantified in Section 3.3). Traces A–C depict the control samples of neat kerosene, kerosene with TOPO surfactant, and NC particles added with surfactant. Notably, the burning rate is only marginally affected by NC addition alone and visible effects of the surfactant and NC particles are limited to the end stage of droplet combustion.

Combustion traces D–G in Fig. 3 illustrate the effects of oxide addition as nanoparticles. Longer traces suggest slower burning rates but quantification in Section 3.3 shows near zero effect, with slight burning rate increases (most significant for  $\text{KIO}_4$ ). Slightly longer traces are thought to be from small density variations with the solid additives which, with constant droplet volume, decreases the significance of drag compared to droplet inertia. It is possible that such slightly higher droplet velocities near termination marginally increase burning rates when solid additives are included by promoting aerodynamic mixing compared to liquid-only samples. This effect is estimated to be small relative to the effects of MP additives and comparable to the experimental error. The droplet combustion of all oxide-only formulations remains unaffected for the first approximately 50% of their lifetimes.  $\text{CuO}$  incites droplet disruptions at the earliest point in the droplet lifetime with the most widely dispersed activity and increased flame emission. Initial disruptions of  $\text{KIO}_4$ , while appearing to occur later and with less flame emission expansion, are of a similar nature to those of  $\text{CuO}$ , characterized by asymmetrical flame plume expansions. As  $\text{KIO}_4$ -laden droplets approach termination, they demonstrate a more swollen emission profile.  $\text{MgO}$  also incites highly emitting disruptions, however they typically only occur in less than ten events in the last roughly 80% of the combustion time, are more symmetrical, high emission, and most prevalent near droplet termination. This is the first indication that  $\text{CuO}$  and  $\text{KIO}_4$  may affect flame chemistry with emerging gas phase agents while  $\text{MgO}$  activity may be limited to when flame and solid particles interact.  $\text{Al}_2\text{O}_3$  shows very small perturbations in the flame but generally only lengthens flame emission near droplet termination, consistent with emission from heated  $\text{Al}_2\text{O}_3$  solid particles remaining as liquid burnout completes.

The last of the combustion traces, H–K, depict NC-bound oxide MPs added to kerosene with surfactant. The drastic shortening of traces H–J demonstrates the significant effect of NC inclusion via MP assembly versus NPs-only. The onset of any droplet/flame disruptions are significantly earlier for NC-bound MP samples in H–J, consistent with observations of nAl MPs [27]. The resulting disruptions are also exaggerated, featuring more widely expanded flame emission for  $\text{CuO}$  and more frequent and brighter emission for  $\text{KIO}_4$  and  $\text{MgO}$  compared to traces D–G.  $\text{Al}_2\text{O}_3$  is the notable exception, showing little to no effect of the NC-bound structure on the activity of the additive, except for added trajectory perturbations consistent with NC-only (in trace C) wherein NC gas generation perturbs the trajectory immediately before droplet termination.

### 3.3. Burning rate measurements

The kerosene/TOPO fuels with MP additives studied include up to 1.15 wt% NC. The burning rates of NC nanoparticle-laden samples up to this loading were assessed without oxides and are shown in Fig. S2. All burning rate data is presented as percent changes in the burning rate constant compared to surfactant-only kerosene ( $K = 2.21 \text{ mm}^2/\text{s}$  with 50 mg/mL TOPO surfactant). NC NPs increase the burning rate linearly by approximately 7% per wt% of NC, agreeing with observations [27] which proposed that NC thermal decomposition, beginning below 200 °C, generates gas within the droplets since combusting liquid droplets heat quickly to the boiling point of the fluid (approximately 220 °C for kerosene). Such generated gas inflates the droplets, thereby increasing liquid surface area for evaporation, and significantly increasing physical mixing of the system. Trace C in Fig. 3 shows these disruptions are most active near droplet termination for NC-only samples. This late disruption onset relative to MP samples in part explains the relatively lower order of magnitude of the burning rate increases for NC alone.

Burning rate effects of the oxide additives are assessed relative to the baseline effects of NC-only and plotted relative to oxygen content for the four oxides in Fig. 4. The calibration curve of NC-only is overlaid on each plot to show the burning rate of NC-only, relative to MP samples with the same amount of NC. With this frame of reference, an obvious benefit of NC-bound MPs is evident for  $\text{CuO}$ ,  $\text{KIO}_4$ , and  $\text{MgO}$  based formulations. Consistent with the combustion traces in Section 3.2,  $\text{Al}_2\text{O}_3$  is the exception to this effect with little to no discernable benefit of the NC-bound MP architecture. Oxide-only NP samples without NC (solid points of Fig. 4) generally increase or minimally affect burning rates. This is in stark contrast with observations of nAl NPs added alone [27] which decreased the burning rate with added nAl loading.  $\text{KIO}_4$  stands out with the highest burning rate increases at and above 0.9 M oxygen (5.6 wt%  $\text{KIO}_4$  NPs) among the oxide-only samples.

The effect of mass loading of MPs is shown in Fig. 5 with the various oxygen contents of the four oxides. With respect to burning rate,  $\text{KIO}_4$  clearly provides the highest overall rate increase. The oxides with the most significant burning rate increases in MPs ( $\text{KIO}_4$  and  $\text{CuO}$ ) are also the two least efficient oxygen carriers by mass.  $\text{MgO}$  and  $\text{Al}_2\text{O}_3$  boast higher oxygen per mass ratios, however, only  $\text{MgO}$  MPs achieve significant burning rate increases.

### 3.4. Direct observation of droplet disruptions

To further investigate the droplet combustion disruptions that emerge upon  $\text{CuO}$ ,  $\text{KIO}_4$ , and  $\text{MgO}$  MP addition, magnified high speed video was taken at the height of the annotation line in Fig. 3. A representative disruption event for  $\text{CuO}/\text{NC}$  MPs is shown in Fig. 6. Image gains are artificially adjusted to keep the droplet frames visible throughout the event. The  $\text{CuO}/\text{NC}$  MP disruption initiates in the second frame of Fig. 6 with a small region of decreased emission in the flame and a spot of orange emission expansion. The region of lower emission behaves like low temperature gaseous species released from within the droplet since in the following frames, it expands upward through the flame and increases emission consistent with the combustion of gaseous species. Concurrently, the initial spot of orange emission first expands outward in the direction of its ejection for 2–3 frames before veering upward, suggesting nontrivial inertia of the emitting species. Predominantly orange emission plumes with faint regions of green near the edges are observed in frames 5–17 in Fig. 6 accompanying the ejection event. Such emission is consistent with that of copper-containing species, confirmed by emission spectroscopy of a passing  $\text{CuO}$  MP-laden droplet shown in Fig. S6 to likely be excited  $\text{CuO}$  and  $\text{CuOH}$  (orange 608 nm and 618 nm doublet, and green 525–555 nm band, respectively). In the fifth frame, this presumed copper species liberation occurs again at a secondary site on the left side of the droplet and together these releases overall create the widespread orange/green emission attached to the droplet flame which is visible on the order of 3 ms. A possible explanation is ejection of particulate  $\text{CuO}$  which decomposes and reduces near and in the flame region thereby affecting gas phase reactions causing the emission increase which lingers around the droplet flame.

Disruptions of  $\text{KIO}_4/\text{NC}$  MPs, represented by Fig. 7, contain notable differences relative to those of  $\text{CuO}$  MPs. First, the droplet flame in the absence of a large disruption is unsteady compared to the flame with  $\text{CuO}$  MPs (seen steady in the first frame of Fig. 6 compared to the deformed flame shape for  $\text{KIO}_4$  MPs shown in the first frame of Fig. 7). The timescale of these small flame perturbations for  $\text{KIO}_4$  MPs is short, on the order of one frame or less (166  $\mu\text{s}$ ), and are possibly due to heterogeneous oxygen release from the droplet by  $\text{KIO}_4$  decomposing near the droplet surface. Larger disruptions occurring concurrently are similar to gas ejections observed for  $\text{CuO}$  MPs and in [27], exemplified in

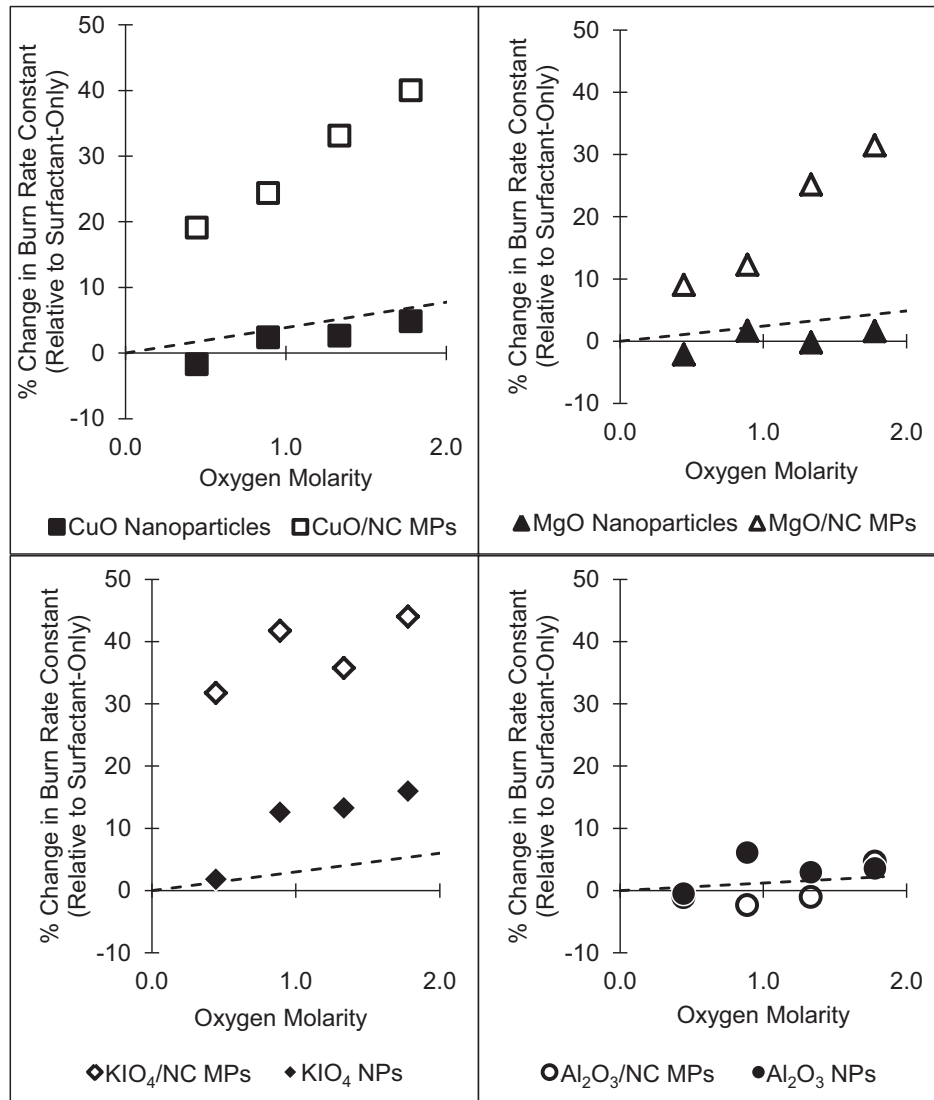


**Fig. 4.** Burning rate effects of CuO, MgO, KIO<sub>4</sub>, and Al<sub>2</sub>O<sub>3</sub> nanoparticles and NC-bound MPs. Dotted lines are the NC-only control fit scaled to correspond to NC content in the MPs at those oxygen molarities. NC oxygen content is not considered.

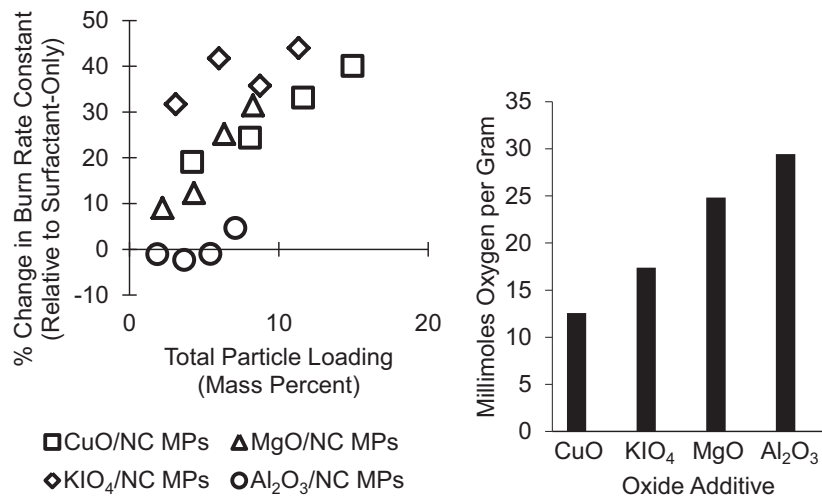


**Fig. 5.** Burning rate effects of all mesoparticle additives versus mass percent particle loading and oxygen carrying efficiency of each oxide.

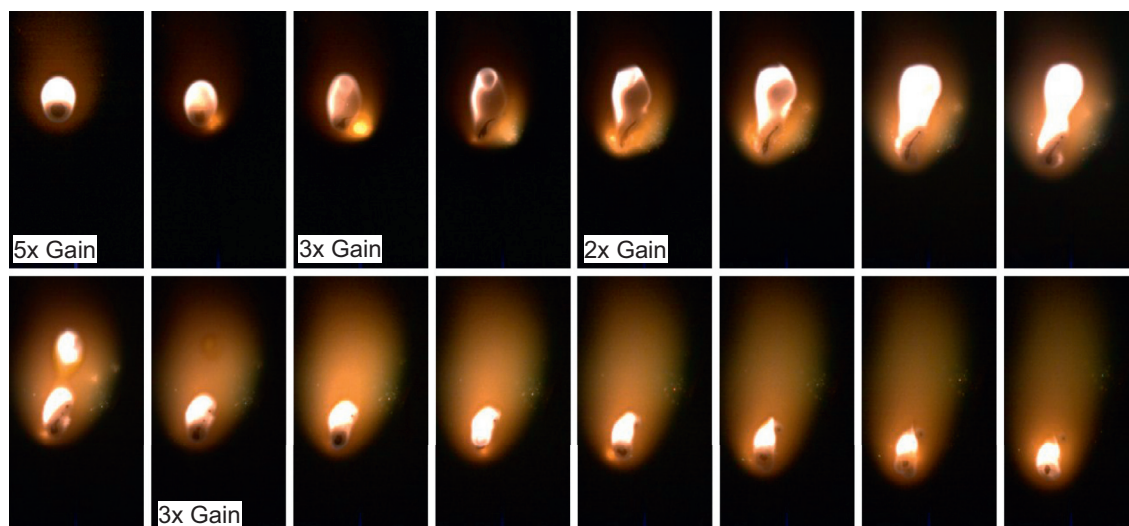


**Fig. 6.** Representative swelling/eruption event during combustion of CuO/NC MPs in kerosene/TOPO. Brightness is artificially increased for visibility as labeled on the first frame of each gain adjustment setting. 166  $\mu$ s image period.

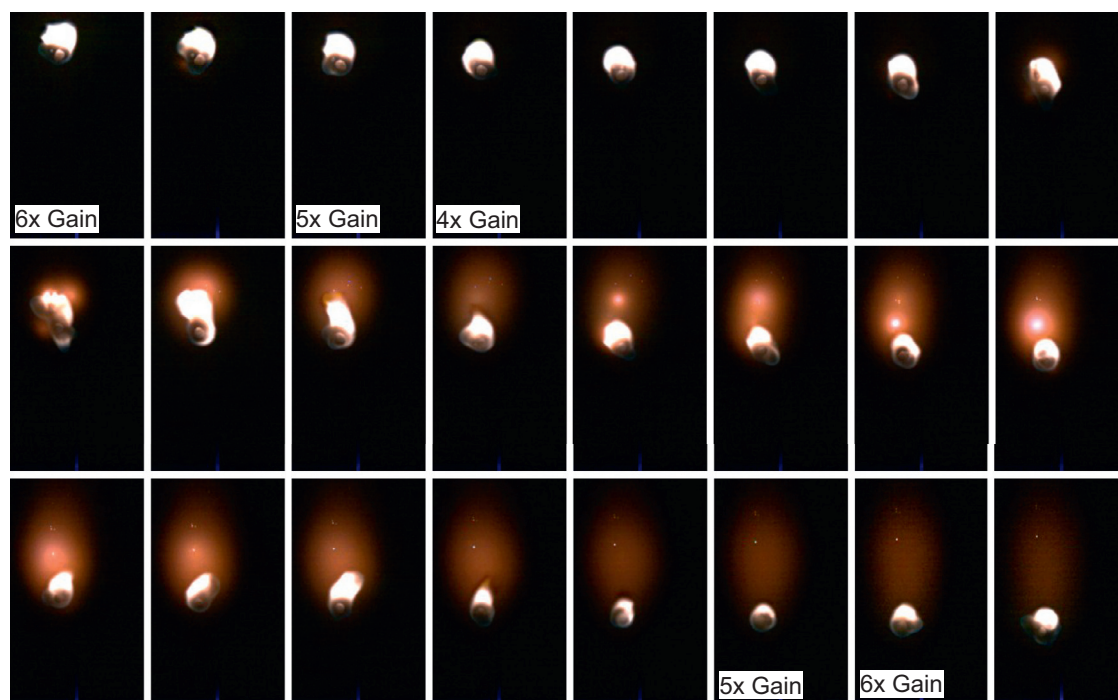


**Fig. 7.** Combustion of KIO<sub>4</sub>/NC MPs in kerosene/TOPO. Brightness is artificially increased for visibility as labeled on the first frame of each gain adjustment setting. First two frames show a companion microdroplet to the left and above the main droplet, which generates the orange emission detached from the main droplet flame as it combusts fully. 166  $\mu$ s image period.

the seventh frame of Fig. 7 at the bottom right of the droplet. However, compared to those of CuO MPs these events are smaller, occur more frequently, and have little to no spectral effect on the flame emission. Orange-violet emission beginning in the ninth frame is not attached to the droplet flame (like the emission expansion of the CuO MP disruption), but rather seems to emanate from a small companion droplet visible left of the main drop in the first three frames. This companion droplet, formed from a prior disruption, enters the flame zone near frame nine and incites the increased emission above the flame. Two other examples of companion droplet liberation and combustion are seen in frames 13 and 15.

MgO/NC MP disruptions, such as those depicted in Fig. S4, resemble those of CuO MPs in that the droplet flame is steady in the

absence of a disruption and the perturbations are characterized by gas eruptions, albeit with significantly smaller flame emission expansions. However, MgO MPs show small spots of emission consistent with particle release more prevalently than CuO MPs, shown in Fig. S5. These particle spot emissions survive in the flame zone significantly longer than any particle emission observed for CuO or KIO<sub>4</sub> MPs.

### 3.5. Thermodynamic considerations

To assess possible reduction of the oxides by reaction with combustion species, NASA CEA was used to generally investigate thermodynamic equilibrium species of stoichiometric combustion of RP-1 and O<sub>2</sub> with small amounts of CuO, MgO, or Al<sub>2</sub>O<sub>3</sub> added

**Table 2**

Results of NASA CEA equilibrium calculations for constant enthalpy, constant temperature stoichiometric RP-1/O<sub>2</sub> with additives (added as 1% of the oxidizer by mass).

Additive	None (RP-1/O <sub>2</sub> )	CuO	MgO	Al <sub>2</sub> O <sub>3</sub>			
Equil. T (K)	3110	3105	3097	3103			
Equil. mole fractions containing additive metal		Cu CuO CuOH	2.3E-03 3.8E-05 1.0E-05	Mg MgO MgOH Mg(OH) <sub>2</sub>	2.2E-03 1.9E-03 3.4E-04 2.4E-04	Al <sub>2</sub> O <sub>3(L)</sub> AlOH AlO Al(OH) <sub>2</sub> AlO <sub>2</sub> HAlO <sub>2</sub> Al(OH) <sub>3</sub> Al	1.1E-03 1.0E-03 3.0E-04 3.9E-05 3.0E-05 2.9E-05 2.5E-05 1.5E-05

**Table 3**

Reaction thermodynamics of oxide reduction by CO and H<sub>2</sub>.

	$\Delta H$ kJ/mol	$\Delta S$ kJ/mol K	$\Delta G$ (300 K) kJ	T ( $\Delta G=0$ ) K
<b>Reduction by CO</b>				
CuO <sub>(s)</sub> + CO = Cu + CO <sub>2</sub>	210	0.1395	169	1508
CuO <sub>(s)</sub> + CO = Cu <sub>2</sub> O <sub>(l)</sub> + CO <sub>2</sub>	-83	0.0601	-101	
MgO <sub>(s)</sub> + CO = Mg + CO <sub>2</sub>	466	0.1378	425	3381
Al <sub>2</sub> O <sub>3(s)</sub> + CO = AlO + CO <sub>2</sub>	1460	0.1835	1405	7954
KIO <sub>4(s)</sub> + CO = KIO <sub>3(s)</sub> + CO <sub>2</sub>	-326	-0.0081	-324	
<b>Reduction by H<sub>2</sub></b>				
CuO <sub>(s)</sub> + H <sub>2</sub> = Cu + H <sub>2</sub> O	252	0.1815	197	1386
CuO <sub>(s)</sub> + H <sub>2</sub> = Cu <sub>2</sub> O <sub>(l)</sub> + H <sub>2</sub> O	-42	0.1021	-72	
MgO <sub>(s)</sub> + H <sub>2</sub> = Mg + H <sub>2</sub> O	507	0.1798	453	2820
Al <sub>2</sub> O <sub>3(s)</sub> + H <sub>2</sub> = AlO + H <sub>2</sub> O	1501	0.2255	1433	6655
KIO <sub>4(s)</sub> + H <sub>2</sub> = KIO <sub>3(s)</sub> + H <sub>2</sub> O	-285	0.0339	-295	

(KIO<sub>4</sub> thermodynamic properties unavailable in CEA) [36]. Results of these calculations are given in Table 2. Equilibrium calculations show that the addition of the metal oxides is insufficient to appreciably impact the adiabatic flame temperature. Considering the concentration of the reduced metal vs. its parent metal oxide shows that while CuO undergoes significant decomposition at flame temperatures, alumina is relatively inert and MgO is in between. This is consistent with the observed effect on burning rate and the visual observations of droplet combustion and disruptions.

Another way of considering this is to assess the likelihood of redox reaction between the oxides and major reducing gases expected in the rich zone of the diffusion flame (i.e. CO and H<sub>2</sub>). For reactions with positive free energies at room temperature, the temperature at which the free energy equals zero is listed in Table 3. These reduction reaction onset temperatures show that Al<sub>2</sub>O<sub>3</sub> reduction by combustion species is not thermodynamically favorable at reasonably physical temperatures (<6600 K). KIO<sub>4</sub> and partial CuO reduction by combustion species is thermodynamically favored down to room temperature, with full CuO reduction to Cu favored above 1300–1600 K. MgO reduction is only thermodynamically spontaneous above 2820 K for reduction by H<sub>2</sub> (3381 K for CO). This is near possible flame temperatures for kerosene/oxygen as suggested by flame spectroscopy fits to Planck's Law in Figs. S7–S11 and Table S1. Most reduction reactions are endothermic except for those of KIO<sub>4</sub>.

Flame emission spectroscopy results shown in Fig. S6 reveal emission peaks attributed to CuOH/CuO, K, and MgOH/MgO/Mg for CuO, KIO<sub>4</sub>, and MgO additives respectively. Peaks near 589 nm and 767 nm are strong sodium and potassium lines, the potassium in the CuO spectra attributed to slight contamination by KIO<sub>4</sub> in the droplet generation assembly. Atomic lines of CuO and MgO support the notion that the additives reach the high temperature flame region, despite the expectation that CuO also undergoes concurrent thermal decomposition. Mg emission is evidence of MgO reduction reactions to a small degree considering the weak intensity of

the Mg peak. Both CuO and MgO form hydroxides in the flame by reaction with H. Flame temperatures estimated by fitting Plank's law to the collected spectral intensity are shown on the respective spectral plots in Figs. S7–S11, suggesting flame temperatures in the range of 2900 K–3300 K. However, the uncertainty in this measurement is estimated to be at least 200 K and the model does not consider non-blackbody emissivity of the flame species and emitting particulates. The estimate does however provide evidence that the MgO reduction reactions considered in Table 3 are possible in the combustion of the kerosene droplets in oxygen.

### 3.6. Proposed mechanisms

#### 3.6.1. Role of NC in MP additive effects

The NC-bound mesoparticle architecture has been shown in [27] to be beneficial for burning rate enhancement by addition of energetic solids to kerosene. This nanoparticle preassembly controls the primary particle agglomeration in a structure that is bound by NC which itself can decompose at low temperature (~200 °C) exothermically releasing gas and disassembling the agglomerate. This architecture also demonstrated much improved colloidal stability enabling longer particle settling times and higher maximum testable loadings. In this study, CuO, KIO<sub>4</sub>, and MgO additives all exhibit drastically higher burning rate constants in kerosene when incorporated into NC-bound MPs. These observations can be explained by the notion of a positive feedback loop first presented in our previous study [27]. As NC within the combusting droplets decomposes, generated gas swells the droplet. The resulting enlargement of liquid surface area exposed to the flame contributes to higher gasification rates of the droplet (and therefore higher burning rates) [27]. Both magnified videography in this study and results of [27] show clear disruptions caused by gas releases in MP samples. Once the first of these disruptions occurs, the resulting droplet deformation and increased mixing promote mass and thermal transfer rates. Disruptions also transport addi-

tive particles or decomposition products to the flame region. For CuO, KIO<sub>4</sub>, MgO, and nAl in [27], these additives are shown to have combustion promoting effects by releasing oxygen on the fuel rich side of the flame or adding to the calorific output (for nAl). Increased mass and heat transfer together with faster combustion reaction rates or calorific output would increase the rate at which NC remaining within the condensed phase decomposes to repeat this cycle. Therefore, this primary mechanism forms a self-accelerating positive feedback loop consistent with the earlier and more frequent disruptions observed for NC-bound MP-laden droplets.

Notably, Al<sub>2</sub>O<sub>3</sub> MPs had minimal effect on burning rates and showed no added droplet disruptions relative to NC-only control samples, therefore representing a physical control group. Two factors likely contribute to this lack of an apparent NC decomposition feedback loop mechanism in this case: the high thermal stability of Al<sub>2</sub>O<sub>3</sub> and its high heat capacity, approximately twice that of CuO, MgO, or nAl (KIO<sub>4</sub> has a higher heat capacity than Al<sub>2</sub>O<sub>3</sub> but easily decomposes before surviving in the flame for appreciable time). Both such characteristics of Al<sub>2</sub>O<sub>3</sub> likely slow or interrupt the chain of events proposed necessary to form a feedback loop between a gas ejection, the resulting droplet and combustion disruption effects, and subsequent occurrences of gas ejection brought on by those effects.

### 3.6.2. Oxide-specific activity

With an oxygen release temperature (~1000 K depending on heating rate) significantly below the flame temperature, CuO will act as an oxygen donor. Furthermore, reduction of CuO to Cu by CO and H<sub>2</sub> is thermodynamically favored in the flame. Therefore, CuO likely undergoes both thermal decomposition and direct reduction once it enters the flame region upon droplet disruptions. Such decomposition effectively delivers gas phase oxygen to the fuel rich side of the flame. These two pathways fit droplet disruption observations discussed in Section 3.4 wherein evidence of both gas phase reaction (suggested by emission attached to the droplet flame) and particle existence within the flame at disruption onset are attributed to the CuO additive.

While onset of KIO<sub>4</sub>/NC MP disruptions are consistent with gas ejections caused by phase change and/or NC decomposition within the droplet, the KIO<sub>4</sub> seems most active either in the absence of such an event (likely by perturbing the droplet flame upon releasing decomposition products) or by entering the flame in a companion droplet generated by secondary atomization during a gas ejection. Such companion droplets combust quickly due to their small size and add to the surface area of condensed species exposed to flame, thereby increasing burning rates. Overall, these disruption characteristics suggest that solid KIO<sub>4</sub> particles likely don't survive decomposition as long as those of CuO. TGA results confirm a lower oxygen release temperature for KIO<sub>4</sub> relative to CuO, in two decomposition steps at 604 K and 830 K. This first oxygen release step would occur in lower temperature regions of the system compared to CuO i.e. closer to the droplet surface, which can explain the steady flame perturbations observed. The second decomposition step can account for the added emission from combusting companion droplets, as any remaining KIO<sub>4</sub> or KIO<sub>3</sub> in such droplets decomposes rapidly upon liquid burn-off releasing excited KI species and O<sub>2</sub>.

MgO is unlikely to thermally decompose to release any oxygen at the temperatures reached in this system and instead is thought to only be partially reduced in the flame by high temperature reducing species such as H<sub>2</sub>, as supported by CEA calculations and thermodynamic consideration of redox reactions considered in Section 3.5. This activity agrees with the observations of MgO MP disruptions in that the emission increase around the flame is significantly smaller and lower intensity than that of CuO, which both thermally decomposes and reduces in the flame. The significant

presence of emitting point sources during such disruptions can be explained by condensed phase MgO undergoing reduction in the flame followed by any resulting Mg reoxidizing in the oxygen rich atmosphere outside of the flame while it sustains enough thermal energy to do so from the exothermicity of Mg oxidation.

## 4. Conclusions

CuO/NC, KIO<sub>4</sub>/NC, and MgO/NC mesoparticles loaded up to 14.9%, 11.3%, and 8.3% by weight in kerosene fuel with TOPO surfactant have been shown to increase burning rates 40%, 44%, and 31% respectively compared to the surfactant-only control, while inactive Al<sub>2</sub>O<sub>3</sub>/NC MPs were shown to have minimal effects. These materials also show significant improvement in colloidal stability compared to unassembled nanoparticles. The mechanism by which the NC-bound MP architecture facilitates these effects, presented first in a previous study [27], is supported by these results, in which NC binder decomposes within the droplet to generate droplet-deforming gas ejections, increasing mass and thermal transfer rates, promoting gasification rates, and transporting additive to the flame.

## Acknowledgments

This work was made possible from the support of an Air Force Office of Scientific Research MURI grant and the Defense Threat Reduction Agency. SEM and TEM performed in the UMD AIMLab. Special thanks to Professor Richard Yetter of Penn State University for providing the original droplet combustion tower apparatus.

## Supplementary materials

Supplementary material associated with this article can be found, in the online version, at doi:10.1016/j.combustflame.2017.08.026.

## References

- [1] J. Sabourin, D. Dabbs, R. Yetter, F. Dryer, I. Aksay, Functionalized graphene sheet colloids for enhanced fuel/propellant combustion, *ACS Nano* 3 (2009) 3945–3954.
- [2] J. Sabourin, R. Yetter, B. Asay, J. Lloyd, V. Sanders, G. Risha, S. Son, Effect of nano-aluminum and fumed silica particles on deflagration and detonation of nitromethane, *Propellants Explos. Pyrotech.* 34 (2009) 385–393.
- [3] S. Choi, J. Eastman, Enhancing thermal conductivity of fluids with nanoparticles, *ASME International Mechanical Engineering Congress & Exposition*, San Francisco, CA, 1995.
- [4] P. Choudhury, Slurry fuels, *Prog. Energy Combust. Sci.* 18 (1992) 409–427.
- [5] R. Yetter, G. Risha, S. Son, Metal particle combustion and nanotechnology, *Proc. Combust. Inst.* 32 (2009) 1819–1838.
- [6] M. Kao, C. Ting, B. Lin, T. Tsung, Aqueous aluminum nanofluid combustion in diesel fuel, *J. Test. Eval.* 36 (2008) 186–190.
- [7] H. Tyagi, P.E. Phelan, R. Prasher, R. Peck, T. Lee, J.R. Pacheco, P. Arentzen, Increased hot-plate ignition probability for nanoparticle-laden diesel fuel, *Nano Lett.* 8 (2008) 1410–1416.
- [8] R. Mehta, M. Chakraborty, P. Parikh, Nanofuels: combustion, engine performance and emissions, *Fuel* 120 (2014) 91–97.
- [9] V. Sajith, C. Sobhan, G. Peterson, Experimental investigations on the effects of cerium oxide nanoparticle fuel additives on biodiesel, *Adv. Mech. Eng.* (2010) 581407.
- [10] N. Sarvestany, A. Farzad, E. Ebrahimnia-Bajestan, M. Mir, Effects of magnetic nanofluid fuel combustion on the performance and emission characteristics, *J. Dispers. Sci. Technol.* 35 (2014) 1745–1750.
- [11] N. Singh, R. Bharj, Effect of CNT-emulsified fuel on performance emission and combustion characteristics of four stroke diesel engine, *Int. J. Curr. Eng. Technol.* 5 (2015) 477–485.
- [12] B. Van Devener, S. Anderson, Breakdown and combustion of JP-10 fuel catalyzed by nanoparticulate CeO<sub>2</sub> and Fe<sub>2</sub>O<sub>3</sub>, *Energy Fuels* 20 (2006) 1886–1894.
- [13] C. Allen, G. Mittal, C. Sung, E. Toulson, T. Lee, An aerosol rapid compression machine for studying energetic-nanoparticle-enhanced combustion of liquid fuels, *Proc. Combust. Inst.* 33 (2011) 3367–3374.
- [14] X.-t.-f. E, X. Zhi, Y. Zhang, C. Li, J. Zou, X. Zhang, L. Wang, Jet fuel containing ligand-protecting energetic nanoparticles: a case study of boron in JP-10, *Chem. Eng. Sci.* 129 (2015) 9–13.

- [15] J. Sabourin, R. Yetter, V. Parimi, Exploring the effects of nanostructured particles on liquid nitromethane combustion, *J. Propuls. Power* 26 (2010) 1006–1015.
- [16] K. McCown, E. Petersen, Effects of nano-scale additives on the linear burning rate of nitromethane, *Combust. Flame* 161 (2014) 1935–1943.
- [17] Y. Gan, L. Qiao, Radiation-enhanced evaporation of ethanol fuel containing suspended metal nanoparticles, *Int. J. Heat Mass Transf.* 55 (2012) 5777–5782.
- [18] Y. Gan, L. Qiao, Optical properties and radiation-enhanced evaporation of nanofluid fuels containing carbon-based nanostructures, *Energy Fuels* 26 (2012) 4224–4230.
- [19] I. Javed, S. Baek, K. Waheed, G. Ali, S. Cho, Evaporation characteristics of kerosene droplets with dilute concentrations of ligand-protected aluminum nanoparticles at elevated temperatures, *Combust. Flame* 160 (2013) 2955–2963.
- [20] I. Javed, S.W. Baek, K. Waheed, Effects of dense concentrations of aluminum nanoparticles on the evaporation behavior of kerosene droplet at elevated temperatures: the phenomenon of microexplosion, *Exp. Therm. Fluid Sci.* 56 (2014) 33–44.
- [21] I. Javed, S. Baek, K. Waheed, Autoignition and combustion characteristics of heptane droplets with the addition of aluminium nanoparticles at elevated temperatures, *Combust. Flame* 162 (2015) 191–206.
- [22] S. Tanvir, L. Qiao, Effect of addition of energetic nanoparticles on droplet-burning rate of liquid fuels, *J. Propuls. Power* 31 (2015) 408–415.
- [23] Y. Gan, Y. Lim, L. Qiao, Combustion of nanofluid fuels with the addition of boron and iron particles at dilute and dense concentrations, *Combust. Flame* 159 (2012) 1732–1740.
- [24] Y. Gan, L. Qiao, Evaporation characteristics of fuel droplets with the addition of nanoparticles under natural and forced convections, *Int. J. Heat Mass Transf.* 54 (2011) 4913–4922.
- [25] I. Javed, S. Baek, K. Waheed, Evaporation characteristics of heptane droplets with the addition of aluminum nanoparticles at elevated temperatures, *Combust. Flame* 160 (2013) 170–183.
- [26] A. Miglani, S. Basu, Coupled mechanisms of precipitation and atomization in burning nanofluid fuel droplets, *Sci. Rep.* 5 (2015). <https://www.ncbi.nlm.nih.gov/pmc/articles/PMC4597229/>.
- [27] P.M. Guerieri, J.B. DeLisio, M.R. Zachariah, Nanoaluminum/Nitrocellulose microparticle additive for burn enhancement of liquid fuels, *Combust. Flame* 176 (2017) 220–228.
- [28] H. Wang, G. Jian, S. Yan, J.B. DeLisio, C. Huang, M.R. Zachariah, Electro spray formation of gelled nano-aluminum microspheres with superior reactivity, *ACS Appl. Mater. Interfaces* 5 (2013) 6797–6801.
- [29] H. Wang, G. Jian, G.C. Egan, M.R. Zachariah, Assembly and reactive properties of Al/CuO based nanothermite microparticles, *Combust. Flame* 161 (2014) 2203–2208.
- [30] R.J. Jacob, B. Wei, M.R. Zachariah, Quantifying the enhanced combustion characteristics of electro spray assembled aluminum mesoparticle, *Combust. Flame* 163 (2016) 281–289.
- [31] G. Young, H. Wang, M.R. Zachariah, Application of nano-aluminum/nitrocellulose mesoparticle in composite solid rocket propellants, *Propellants Explos. Pyrotech.* 40 (2015) 413–418.
- [32] G.C. Egan, K.T. Sullivan, T. LaGrange, B.W. Reed, M.R. Zachariah, *J. Appl. Phys.* 115 (2014) 084903.
- [33] K. Okuyama, I.W. Lenggoro, Preparation of nanoparticles via spray route, *Chem. Eng. Sci.* 58 (2003) 537–547.
- [34] P.M. Guerieri, S. DeCarlo, B. Eichhorn, T. Connell, R.A. Yetter, X. Tang, Z. Hicks, K.H. Bowen, M.R. Zachariah, Molecular aluminum additive for burn enhancement of hydrocarbon fuels, *J. Phys. Chem. A* 119 (2015) 11084–11093.
- [35] W. Zhou, J.B. DeLisio, X. Wang, M.R. Zachariah, Reaction mechanisms of potassium oxysalts based energetic composites, *Combust. Flame* 177 (2017) 1–9.
- [36] B.J. McBride, S. Gordon, NASA RP-1311, NASA, 1996.